Dual-Band Metasurface Antenna Based on Characteristic Mode Analysis

Huawei Zhuang[1, *], Honghao Tan[1], Changyong Liu[1], Fei Li[1], Wei Ding[1], Changbin Tian[1], and Fanmin Kong[2]

Abstract—A dual-band metasurface antenna is designed consisting of three-layer metal patches and two-layer dielectric substrates. To facilitate the modal analysis of the metasurface, Characteristic Mode Analysis (CMA) is used to analyze the metasurface antenna with 4×4 rectangular patches, and the performance of the antenna is optimized based on the Modal Significance (MS) curves. In order to excite the current of different characteristic modes at certain frequencies, symmetric resonant arms and cross-shaped impedance matching converters are used in the feeding structure. The measured results are consistent with the simulated values, and the designed antenna can yield gains of $7.67\,\mathrm{dBi}$ at $3.5\,\mathrm{GHz}$ and $7.28\,\mathrm{dBi}$ at $4.9\,\mathrm{GHz}$, which provides the potential applications in 5G and other wireless communications.

1. INTRODUCTION

With the development of high-speed and multi-functional applications in wireless communication technology, multi-band antennas become a trend for future antenna design [1, 2]. Among multi-band antennas, microstrip antennas have the advantages of low profile and compact structure with a wide range of scenarios including smartphones [3], routers [4], base stations [5], etc. Even so, small gain [6–9], low power capacity [10], high loss [11], and low radiation efficiency [12] also bother the development of microstrip antennas.

Usually, metasurface structure is composed of uniform or nonuniform metal patches with multiple unit cells [13], which can significantly improve the radiation efficiency [14, 15] and operating bandwidth [16, 17]. Thus, metasurface structure is regarded as one of the ideal platforms to design the radiation element of the antenna [18]. In order to facilitate the antenna design, characteristic mode analysis (CMA) method is introduced during the antenna design process, and the values of Modal Significances (MSs) are solved in the desired frequency bands [19, 20]. For example, Li and Chen used CMA to optimize the radiation element structure by tuning metasurface current distributions and obtained three required MSs to achieve dual-band characteristics [21]. Gao et al. investigated the surface current of the radiation elements based on CMA to improve the antenna efficiency [22]. Similarly, Lin and Chen optimized radiation elements by tuning the current distributions based on CMA [23]. The CMA method is also used to increase the antenna bandwidth and suppress unwanted high-order resonant modes [24, 25]. In recent years, advanced materials play a significant role in modern electronic and photonic technologies, providing a highly effective means for the manipulation and control of carriers at terahertz frequencies. With antennas operating at frequencies from gigahertz to terahertz, new two-dimensional materials, such as graphene [26] and Dirac Semimetal [27], can also be used as the radiation element of the antenna.

In this study, a dual-band metasurface antenna is designed based on CMA method with a five-layer structure. The radiation elements contain 4×4 rectangular patches, and the feeding structure consists of symmetric resonant arms and cross-shaped impedance matching converters. The numerical simulation shows that the proposed antenna can operate in the range of $3.43 \sim 3.58\,\text{GHz}$ and $4.61 \sim 5.11\,\text{GHz}$. The measured results are in good agreement with the simulated values. The proposed antenna can be applied to 5G base station, radar, satellite communication, medical imaging, and other wireless communication scenarios. In addition, multi-antenna system based on metasurface antenna can obviously enhance the signal quality of 5G communication networks and realize the multi-beam control by using beam-forming technology.

2. ANTENNA MODEL AND STRUCTURE DESIGN

2.1. Antenna Structure

Figure 1(a) gives the side-view of the metasurface antenna, which is divided into five layers including metasurface, dielectric layer 1, ground plane, dielectric layer 2, and feed structures. The material of dielectric layer 1 is F4BM350 with $\varepsilon_1 = 3.5$, and that of dielectric layer 2 is F4BM265 with $\varepsilon_2 = 2.65$. In addition, the radiation elements in the metasurface composed of 4×4 rectangular patches shown
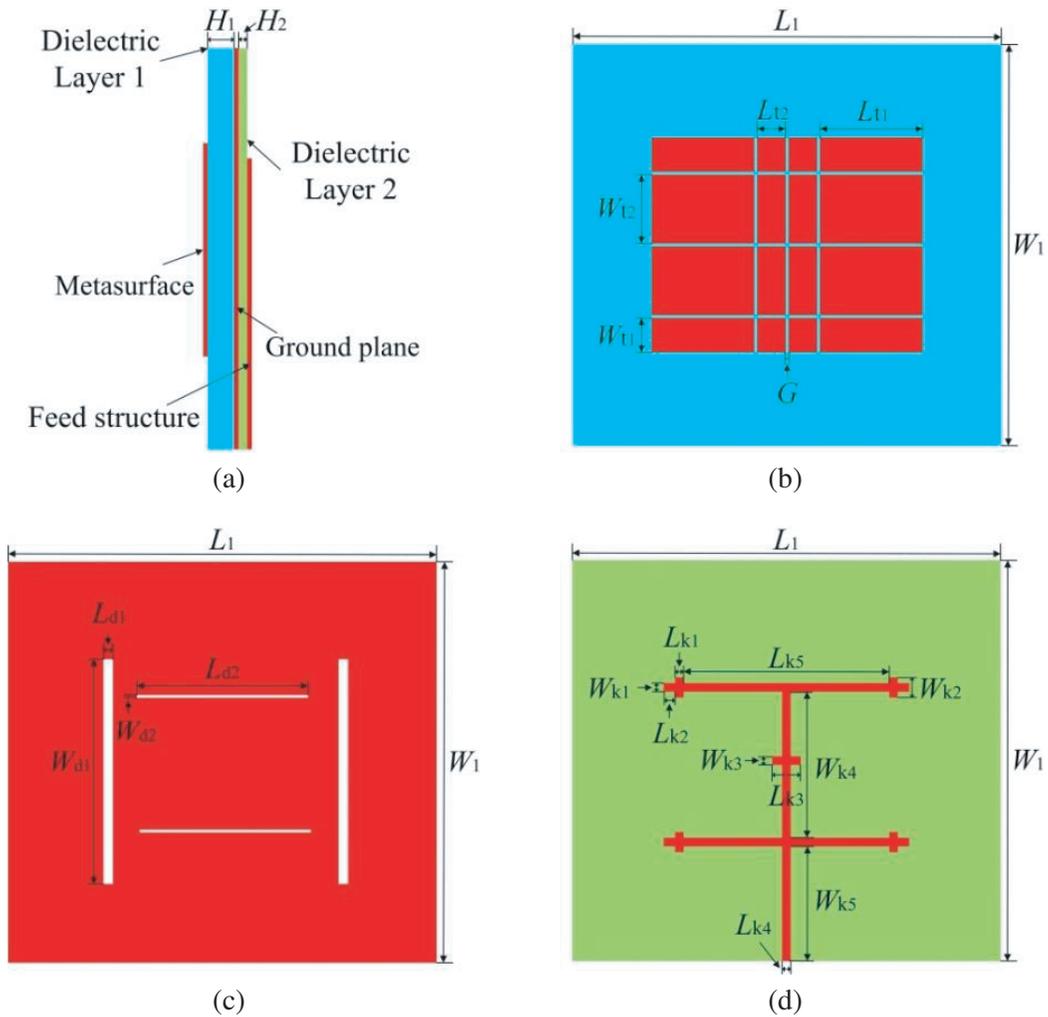

Figure 1. (a) Side-view. (b) Metasurface. (c) Ground plane. (d) Feed structure for the proposed metasurface antenna.

in Fig. 1(b), the coupling apertures on the ground plane shown in Fig. 1(c), and the feed structure shown in Fig. 1(d) are used to excite the radiation energy in the metasurface. The detailed structure parameters of the metasurface antenna are shown in Table 1.

Table 1. Detailed structure parameters of the metasurface antenna.

Parameter	H_1	H_2	G	L_1	L_{t1}	L_{t2}	L_{d1}	L_{d2}
Size (mm)	4.6	0.8	0.5	75	18	5	1.6	30
Parameter	L_{k1}	L_{k2}	L_{k3}	L_{k4}	L_{k5}	W_1	W_{t1}	W_{t2}
Size (mm)	1.5	2	5	1.5	36	8	6	12
Parameter	W_{d1}	W_{d2}	W_{k1}	W_{k2}	W_{k3}	W_{k4}	W_{k5}	
Size (mm)	39.2	0.5	1.5	3.5	1.5	27	20	

2.2. Design and Optimization of Metasurface Based on CMA

The metasurface of the proposed antenna is composed of 4×4 rectangular patches, which can obtain high gain and optimal radiation efficiency. By analyzing the MSs values and the characteristic currents at different characteristics modes, we can derive the desired radiation characteristics at a certain working frequency. During the process of CMA analysis, the dielectric layer beneath the metasurface is regarded as an infinite plane. The effect of modal current J_n in the total current can be characterized by the mode weighting factor [21]

$$\alpha_n = 1/(1 + j\lambda_n) \int J_n \cdot E_i ds \qquad (1)$$

where λ_n is the eigenvalue of the modal current J_n, E_i the applied E field, and S the surface of the conductor area. In addition, MS and modal excitation coefficient are defined as

$$MS = 1/|1 + j\lambda_n| \qquad (2)$$

$$V_i = \int J_n \cdot E_i ds \qquad (3)$$

The MS values at different frequencies can be optimized by tuning the size and position of the radiation patches. As shown in Fig. 2, the first five MSs $J_1 \sim J_5$ are derived in the frequency range from 2.5 GHz to 6.5 GHz. It is obvious that the resonant points of modal currents J_1 and J_3 are around 3.5 GHz, and the maximum value of J_5 is in the vicinity of 4.9 GHz. The surface current distributions and the
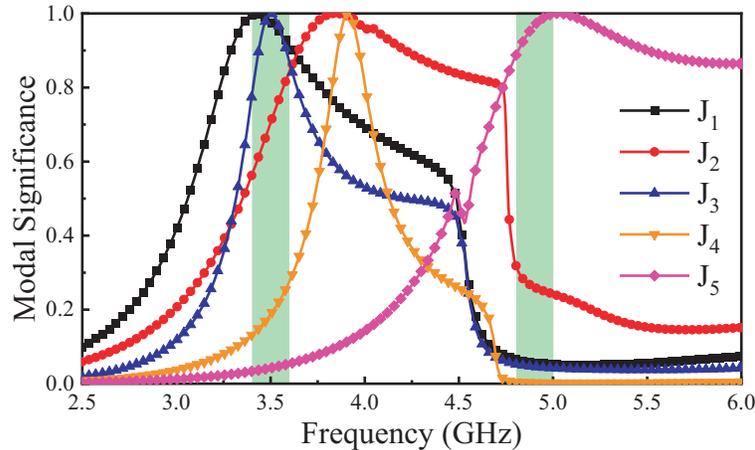

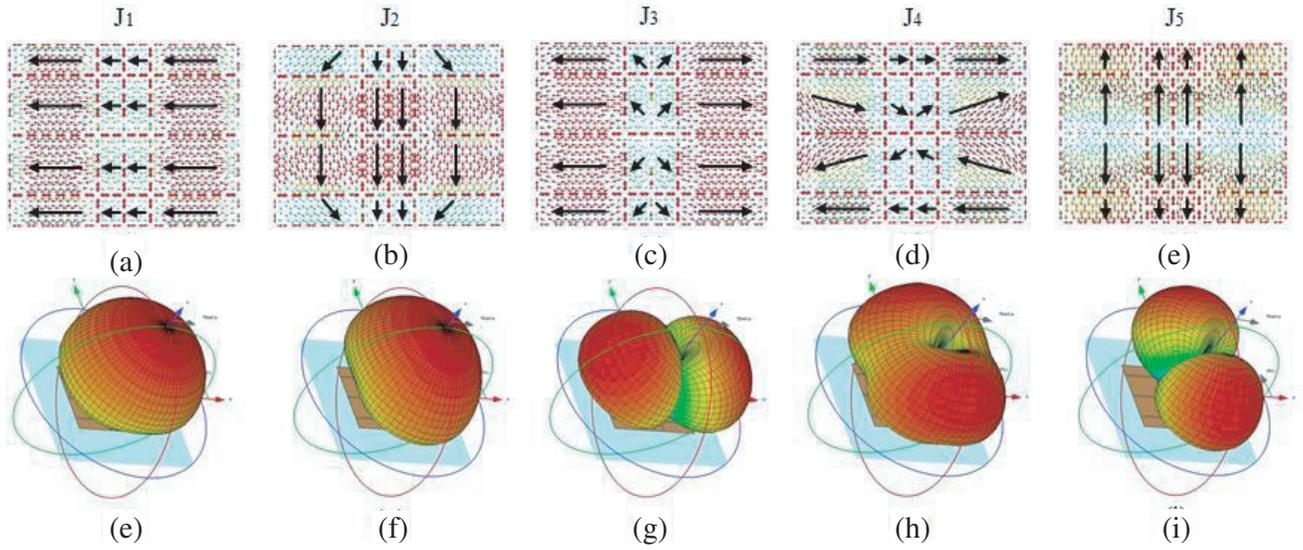**Figure 2.** MS curves of the modes $J_1 \sim J_5$.

Figure 3. Modal currents and radiation patterns of Modes $J_1 \sim J_5$ of the radiation elements.

corresponding radiation patterns of $J_1 \sim J_5$ are shown in Fig. 3. Even though the maximum values of J_1 and J_3 concentrate on the left and right sides of the radiation elements, the modal currents J_1 and J_3 have different radiation characteristics shown in Figs. 3(f) and (h). For J_2, the maximum current is distributed at the central region of the radiation elements, which can produce the perfect unidirectional radiation in Fig. 3(g). For J_4 and J_5, due to the opposite current directions in the left and right of the radiation elements, the maximum radiation appears at the upper and lower sides of the radiation elements.

As we know, the MS currents and the corresponding radiation patterns are determined by the structure parameters of the metasurface. Then, we can tune the parameters to obtain the desired MS values at different modal currents. Fig. 4 gives the variation of the MS curves for modal current J_3 at $L_{t1} = 16 \sim 20\,\mathrm{mm}$ and J_5 at $W_{t1} = 4 \sim 8\,\mathrm{mm}$, respectively. It can be observed from Fig. 4(a) that with the increase of L_{t1}, the resonance frequency of MS curves gradually moves to the lower frequency band. As can be seen from Fig. 4(b) that with the increase of W_{t1}, the resonance frequency of the MS curves
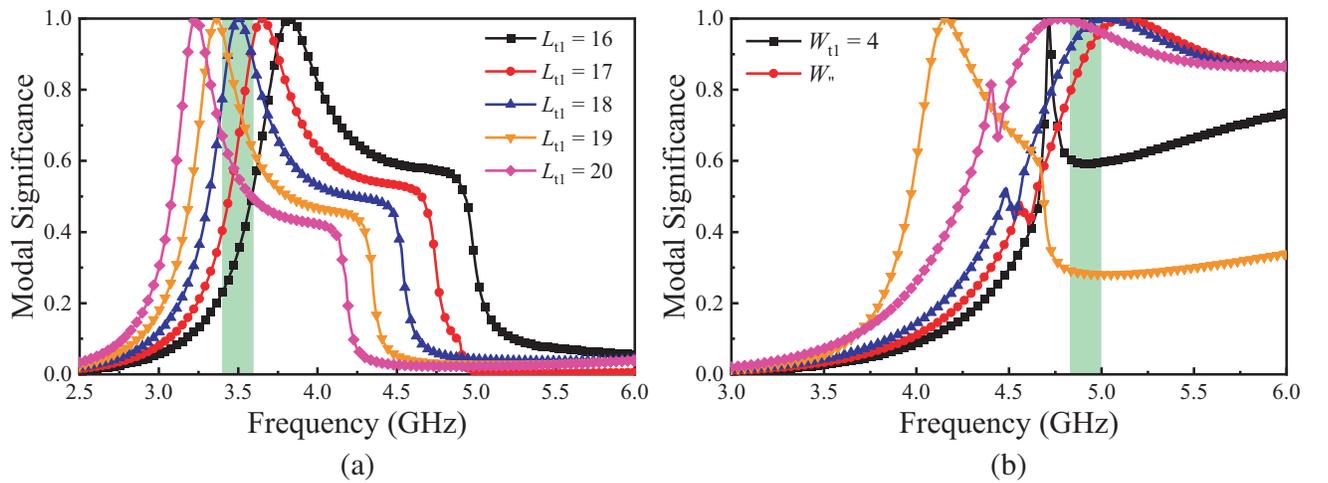

Figure 4. The variation of MS curves for modal current (a) J_3 at $L_{t1} = 16 \sim 20\,\mathrm{mm}$ and (b) J_5 at $W_{t1} = 4 \sim 8\,\mathrm{mm}$.

for J_5 vary irregularly and attain $4.9\,\text{GHz}$ at $W_{t1} = 6\,\text{mm}$. To obtain the dual-band characteristics in the vicinity of $3.5\,\text{GHz}$ and $4.9\,\text{GHz}$, $L_{t1} = 18\,\text{mm}$ and $W_{t1} = 6\,\text{mm}$ are chosen in the following discussion.

2.3. Design and Optimization of the Feed Structure

In order to obtain the desired resonant frequencies at $3.5\,\text{GHz}$ and $4.9\,\text{GHz}$, the appropriate modal currents should be excited, and the unnecessary modal currents are suppressed as much as possible. According to the MS curves distribution in Fig. 2, J_1, J_3, and J_5 are selected to generate the desired frequencies. Based on the current distributions from Fig. 3, the feed aperture in the ground plane should be positioned at the maximum current distribution in the metasurface radiation elements. The apertures in horizontal direction are used to excite modal currents J_1 and J_3 at $3.5\,\text{GHz}$, and the apertures in vertical direction are selected to excite J_5 at $4.9\,\text{GHz}$, as shown in Fig. 1(c). Fig. 5 gives two different feeding apertures and the corresponding S-parameter curves. Compared with the feeding aperture in Fig. 5(a), symmetrical cross-shaped impedance matching conversion in the feed aperture is introduced in Fig. 5(b), and two obvious resonant points in the vicinity of $3.5\,\text{GHz}$ and $4.9\,\text{GHz}$ are excited.
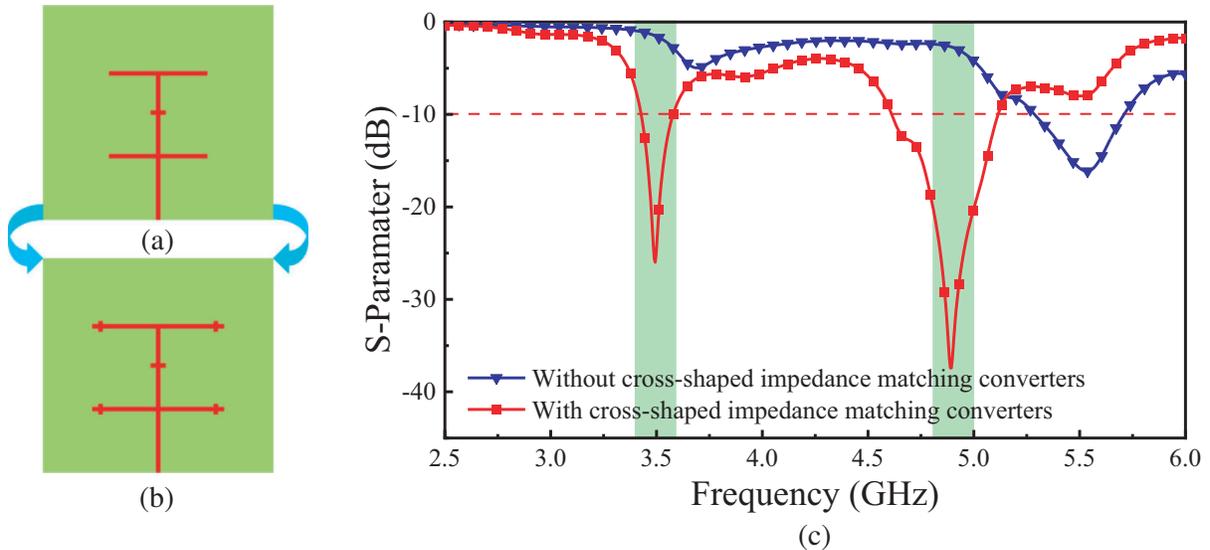

Figure 5. (a) Without and (b) with the cross-shaped impedance matching converters in the feed aperture and (c) the corresponding S-Parameter curves.

Similar to the aperture in the ground plate, the parameter variation in the feed structure can also influence the performance of the metasurface antenna. The detailed structure parameters in the feed structure are shown in Fig. 1(d). Fig. 6(a) shows the S-parameter curves at different W_{k1}. It can be seen that the first resonant point blueshifts obviously as W_{k1} increases, and the second resonant point keeps almost unchanged. Fig. 6(b) shows the variations of the S-parameter at different W_{k5}. With the increase of W_{k5}, the second resonant point blueshifts and attains the minimum at $W_{k5} = 19.25\,\text{mm}$. In addition, as W_{k5} increases, the first band's bandwidth widens concurrently. In order to achieve better performance of the metasurface antenna, $W_{k1} = 1.5\,\text{mm}$ and $W_{k5} = 19.25\,\text{mm}$ are chosen in the following experiment.

2.4. Surface Current Distributions

The current distributions on the metasurface antenna at $3.5\,\text{GHz}$ and $4.9\,\text{GHz}$ are illustrated in Figs. 7(a) and (b), respectively. Due to the intercoupling between modal currents J_1 and J_3 in Fig. 7(a), the current distributions become out-of-phase in the horizontal direction of the middle region. Consequently, the radiation energy caused by the out-of-phase is canceled greatly in the horizontal direction, and the combined current distribution at $3.5\,\text{GHz}$ is along the vertical direction. The combined currents on
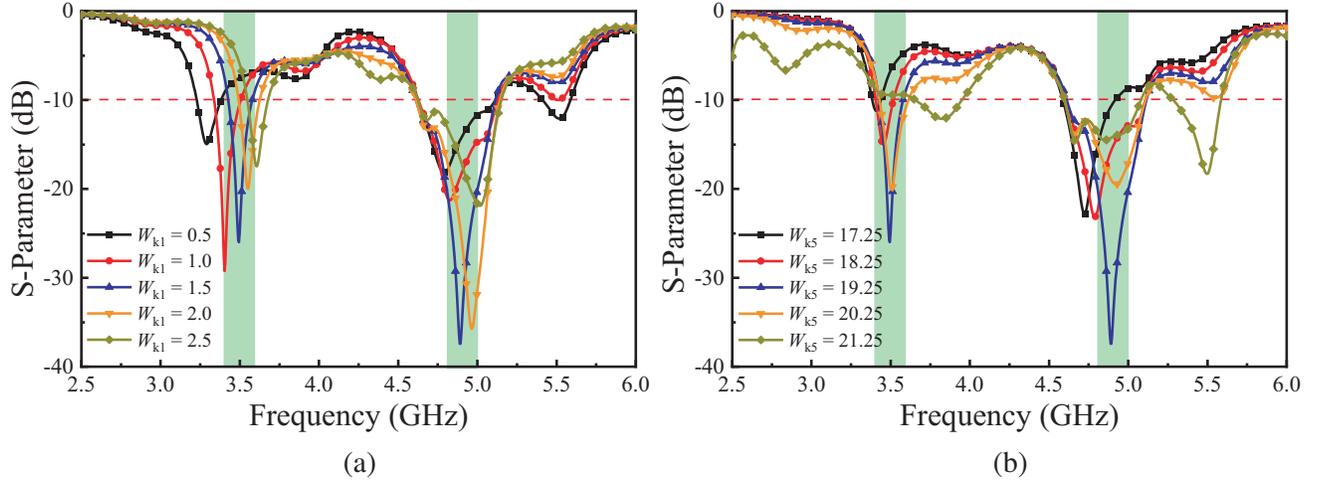
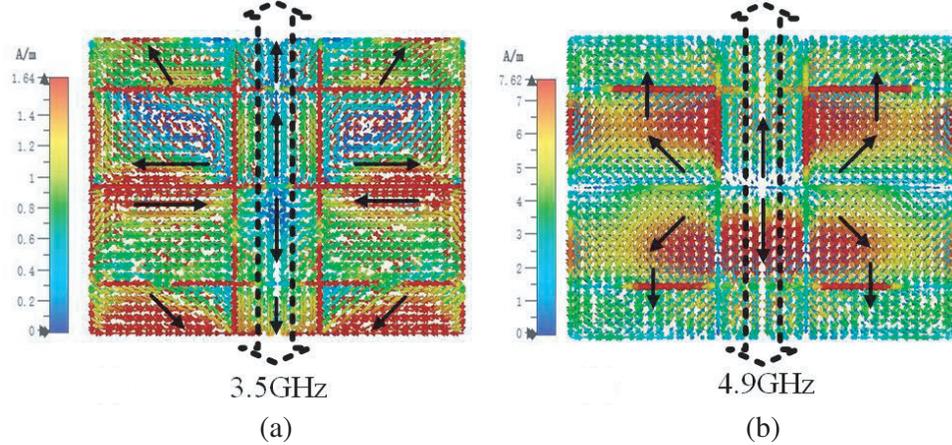**Figure 6.** S-Parameter curves at different (a) W_{k1}, (b) W_{k5}.

Figure 7. Current distributions of the metasurface antenna at (a) $3.5\,\mathrm{GHz}$ and (b) $4.9\,\mathrm{GHz}$.

metasurface radiation elements at $4.9\,\mathrm{GHz}$ are also virtually vertical in Fig. 7(b), going in the same general direction as J_5 at that frequency. Here, J_2 and J_4 are not discussed, because the operating bands are not in the vicinity of $3.5\,\mathrm{GHz}$ and $4.9\,\mathrm{GHz}$.

3. EXPERIMENTAL VALIDATION

3.1. Antenna Manufacture and Measurement

In order to validate the simulation results, the proposed antenna is fabricated and measured. Fig. 8(a) shows the front and back views of the antenna prototype. Fig. 8(b) shows the anechoic chamber, which is used for the antenna testing environment. The vector network analyzer is used to obtain the S-parameter values, and the measured and simulated results are shown in Fig. 8(c). It can be seen that the measured operating bands ($S_{11} \leq -10\,\mathrm{dB}$) are in the range of $3.46 \sim 3.54\,\mathrm{GHz}$ and $4.61 \sim 5.02\,\mathrm{GHz}$, respectively. The measured results are nearly in good agreement with the simulated data. The slight differences between the measured results and simulated values may be caused by the fabrication inaccuracy, test cable, minor tolerance in the dielectric constant of the substrate, and the loss of metasurface metal element.
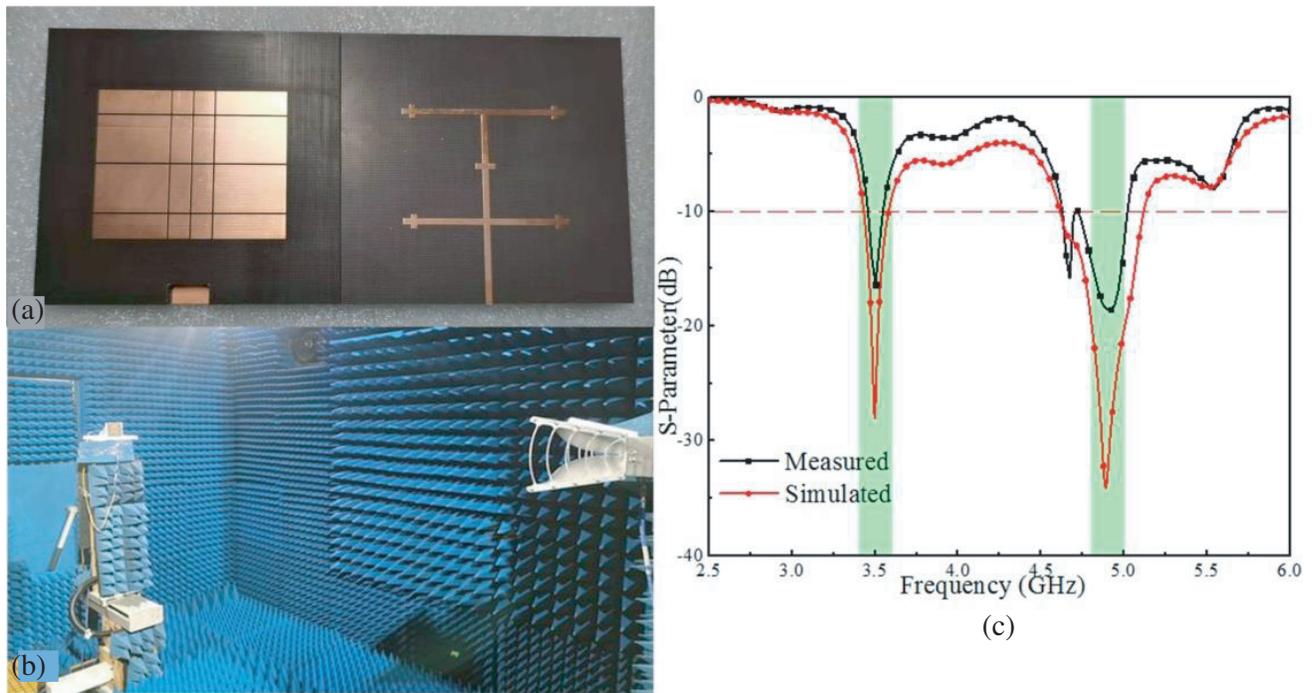
Figure 8. (a) Front and back views of the fabricated antenna prototype. (b) Photograph of the actual measured environment. (c) Simulated and Measured S-Parameters of the metasurface antenna.

3.2. Far-Field Radiation Patterns

In order to further analyze the performance of our proposed metasurface antenna, the far-field radiation patterns and peak gains of the antenna are tested and recorded in an anechoic chamber. Fig. 9 displays the co-polarization and cross-polarization radiation patterns of the metasurface antenna at 3.5 GHz and 4.9 GHz, respectively. It can be observed that the co-polarization patterns present a bidirectional radiation characteristic in the E-plane and a unidirectional radiation characteristic in the H-plane. Thus, the cross-polarization levels at boresight are well suppressed across the operating bands. In

Table 2. Comparison of the proposed antenna with other referred antennas.

| Ref.	Resonant frequency (GHz)	Number of bands	Substrate	Peak Gains (dBi)	Antenna type	Applications
[6]	2.45/3.55/5.5	Triple	FR4	1.22/2.15/4.06	Patch	WLAN WIMAX
[7]	3.6	Single	FR4	2.5	Patch	5G
[8]	2.4/3.6	Dual	FR4	2.6/4.5	Patch	5G/WLAN
[9]	2.4/3.5	Dual	FR4	2.5/4	Patch	5G/ WLAN
[10]	3.6	Single	FR4	4.2	Patch	5G
[11]	3.5	Single	FR4	4	Patch	5G
[12]	3.75	Single	FR4	3	Patch	5G
This work	3.5/4.9	Dual	F4BM265 F4BM350	7.67/7.28	Metasurface	5G
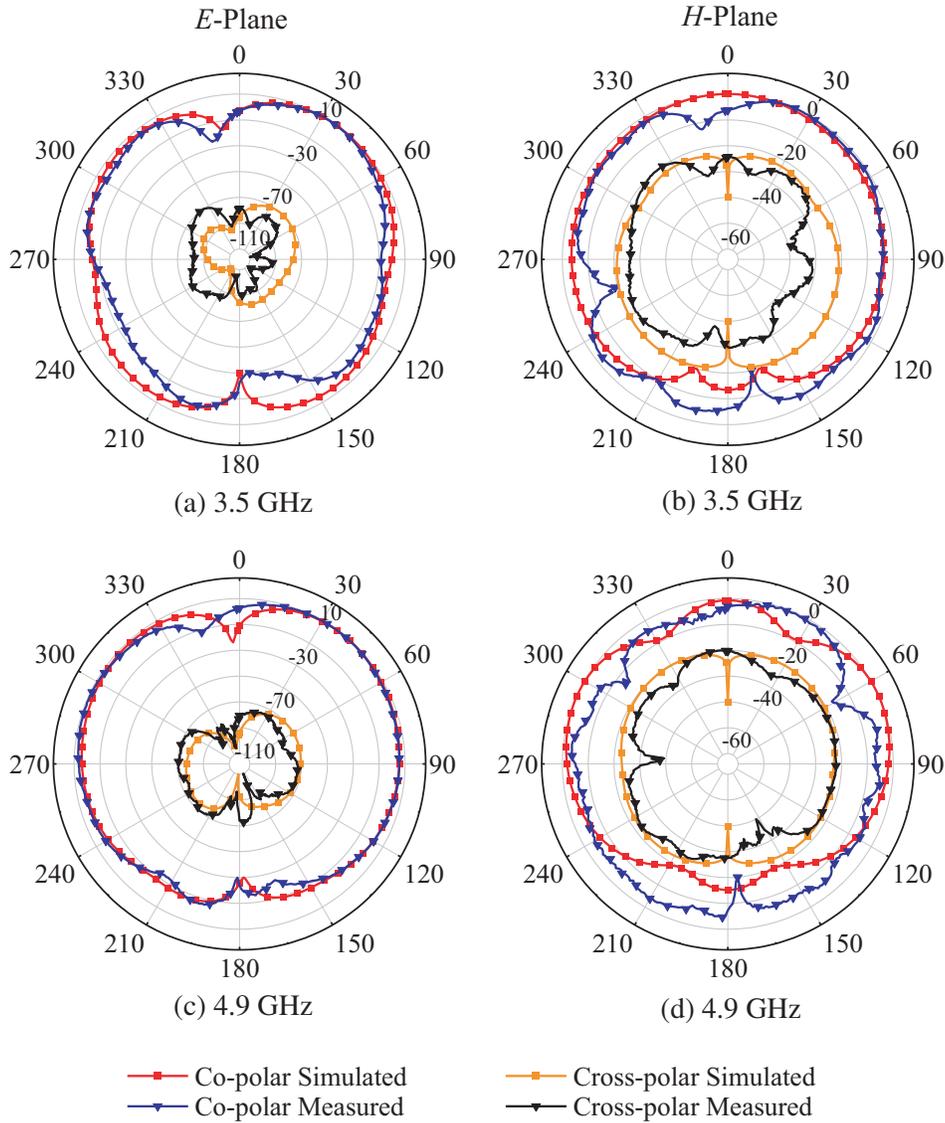
Figure 9. Measured and simulated radiation patterns of the proposed antenna with E-Plane at (a) 3.5 GHz and (c) 4.9 GHz and H-Plane at (b) 3.5 GHz and (d) 4.9 GHz.

addition, the values of co-polarization are more than those of cross-polarization, which satisfies the design standards for the antenna. Due to the welding error, chamber scattering, environmental effects, etc., there are some differences between the measured results and simulated data in the radiation patterns.

3.3. Antenna Gain

The peak gains of the metasurface antenna are shown in Fig. 10. Compared with the simulated peak gains of $5.85 \sim 7.8$ dBi at $3.3 \sim 3.7$ GHz and $5.79 \sim 7.34$ dBi at $4.6 \sim 5.1$ GHz, the measured peak gains are 7.31 dBi at 3.5 GHz and 7.23 dBi at 4.9 GHz, respectively. The results shown in Fig. 10 reveal that the measured and simulated peak gain values show slight differences in tolerable limits. Table 2 shows the comparison of the proposed antenna with other patch antennas. It can be seen that the proposed metasurface antenna can provide higher peak gains than other patch antennas, which can provide more advantages in 5G and other wireless applications.
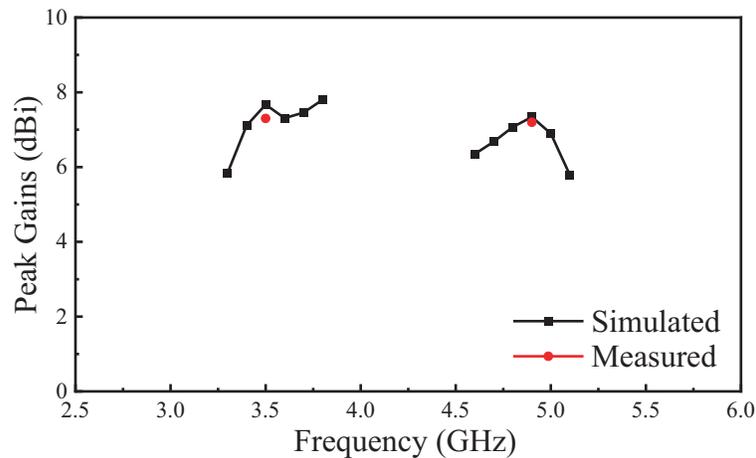
Figure 10. Measured and simulated and peak gains of the metasurface antenna.

4. CONCLUSION

In this paper, a dual-band metasurface antenna based on CMA is proposed and designed, which consists of three-layer metal and two-layer dielectric substrates. With the aid of CMA, the current distributions on the metasurface are analyzed in detail. In order to obtain the appropriate mode current, a feed structure with a symmetrical resonant arm and a cross impedance matching converter is introduced. From the measured and simulated results, the proposed antenna resonates at around 3.5 GHz and 4.9 GHz, both of which lie in the sub-6 GHz band. The measured peak gains can attain 7.31 dBi at 3.5 GHz and 7.23 dBi at 4.9 GHz, respectively. Thus, a conclusion is drawn that the proposed metasurface antenna has enough bandwidth with better bidirectionality and stable gain. The proposed antenna can improve the performance of the communication system and enhance the reliability of signal transmission in 5G or other high-speed wireless communication scenarios.

REFERENCES

1. Lu, X. Y., C. R. Chappidi, X. Wu, and K. Sengupta, "Antenna preprocessing and element-pattern shaping for multi-band mmwave arrays: Multi-port receivers and antennas," *IEEE Journal of Solid-state Circuits*, Vol. 55, No. 6, 1455–1470, 2020.
2. Zhang, J. Y., E. Bjornson, M. Matthaiou, D. W. K. Ng, H. Yang, and D. J. Love, "Prospective multiple antenna technologies for beyond 5G," *IEEE Journal on Selected Areas in Communications*, Vol. 38, No. 8, 1637–1660, 2020.
3. Ban, Y. L., C. Li, C. Y. D. Sim, G. Wu, and K. L. Wong, "4G/5G multiple antennas for future multi-mode smartphone applications," *IEEE Access*, No. 4, 2981–2988, 2016.
4. Abdelghani, A. M., N. F. F. Areed, M. F. O. Hameed, M. A. H. Hindy, and S. S. A. Obayya, "Design of UWB antenna using reconfigurable optical router," *Optical and Quantum Electronics*, Vol. 47, No. 8, 2675–2688, 2015.
5. Anguera, J., A. Andujar, S. Benavente, J. Jayasinghe, and S. Kahng, "High-directivity microstrip antenna with Mandelbrot fractal boundary," *IET Microwaves Antennas & Propagation*, Vol. 12, No. 4, 569–575, 2018.

6. Wang, S. Q., F. M. Kong, K. Li, and L. G. Du, "A planar triple-band monopole antenna loaded with an arc-shaped defected ground plane for WLAN/WiMAX applications," *International Journal of Microwave and Wireless Technologies*, Vol. 13, No. 4, 381–389, 2021.

7. Dwivedi, A. K., A. Sharma, A. K. Pandey, and V. Singh, "Two port circularly polarized MIMO antenna design and investigation for 5G communication systems," *Wireless Personal Communications*, Vol. 120, No. 3, 2085–2099, 2021.

8. Das, G., A. Sharma, and R. K. Gangwar, "Dielectric resonator-based two-element MIMO antenna system with dual band characteristics," *IET Microwaves Antennas & Propagation*, Vol. 12, No. 5, 734–741, 2018.

9. Bharti, G., D. Kumar, A. K. Gautam, and A. Sharma, "Two-port ring-shaped dielectric resonator-based diversity radiator with dual-band and dual-polarized features," *Microwave and Optical Technology Letters*, Vol. 62, No. 2, 581–588, 2020.

10. Saxena, S., B. K. Kanaujia, S. Dwari, S. Kumar, and R. Tiwari, "MIMO antenna with built-in circular shaped isolator for sub-6 GHz 5G applications," *Electronics Letters*, Vol. 54, No. 8, 478–479, 2018.

11. Kumari, T., G. Das, A. Sharma, and R. K. Gangwar, "Design approach for dual element hybrid MIMO antenna arrangement for wideband applications," *International Journal of RF and Microwave Computer-Aided Engineering*, Vol. 29, No. 1, 1–10, 2019.

12. Parchin, N. O., Y. I. A. Al-Yasir, A. H. Ali, I. Elfergani, J. M. Noras, J. Rodriguez, and R. A. Abd-Alhameed, "Eight-element dual-polarized MIMO slot antenna system for 5G smartphone applications," *IEEE Access*, Vol. 7, 15612–15622, 2019.

13. Li, H. P., G. M. Wang, X. J. Gao, J. G. Liang, and H. S. Hou, "An X/Ku-band focusing anisotropic metasurface for low cross-polarization lens antenna application," *Progress In Electromagnetics Research*, Vol. 159, 79–91, 2017.

14. Minatti, G., E. Martini, and D. Maci, "Efficiency of metasurface antennas," *IEEE Transactions on Antennas and Propagation*, Vol. 65, No. 4, 1532–1541, 2017.

15. Lin, F. H. and Z. N. Chen, "A method of suppressing higher order modes for improving radiation performance of metasurface multiport antennas using characteristic mode analysis," *IEEE Transactions on Antennas and Propagation*, Vol. 66, No. 4, 1894–1902, 2018.

16. Liu, S. H., D. Q. Yang, Y. P. Chen, K. Sun, X. K. Zhang, and Y. Xiang, "Design of single-layer broadband omnidirectional metasurface antenna under single mode resonance," *IEEE Transactions on Antennas and Propagation*, Vol. 69, No. 10, 6947–6952, 2021.

17. Li, H. P., G. M. Wang, J. G. Liang, and X. J. Gao, "Wideband multifunctional metasurface for polarization conversion and gain enhancement," *Progress In Electromagnetics Research*, Vol. 155, 115–125, 2016.

18. Li, T. and Z. N. Chen, "Metasurface-based shared-aperture 5G S-/K-band antenna using characteristic modes analysis," *IEEE Transactions on Antennas and Propagation*, Vol. 66, No. 12, 6742–6750, 2018.

19. Liu, S. H., D. Q. Yang, and J. Pan, "A low-profile broadband dual-circularly-polarized metasurface antenna," *IEEE Antennas and Wireless Propagation Letters*, Vol. 18, No. 7, 1395–1399, 2019.

20. Yan, X., Y. Liu, and S. X. Gong, "Design of a wideband omnidirectional antenna with characteristic mode analysis," *IEEE Antennas and Wireless Propagation Letters*, Vol. 17, No. 6, 993–997, 2018.

21. Li, T. and Z. N. Chen, "A dual-band metasurface antenna using characteristic mode analysis," *IEEE Transactions on Antennas and Propagation*, Vol. 66, No. 10, 5620–5624, 2018.

22. Gao, X., G. W. Tian, Z. Y. Shou, and S. M. Li, "A low-profile broadband circularly polarized patch antenna based on characteristic mode analysis," *IEEE Antennas and Wireless Propagation Letters*, Vol. 20, No. 2, 214–218, 2021.

23. Lin, F. H. and Z. N. Chen, "Low-profile wideband metasurface antennas using characteristic mode analysis," *IEEE Transactions on Antennas and Propagation*, Vol. 65, No. 4, 1706–1713, 2017.

24. Gao, G. P., R. F. Zhang, W. F. Geng, H. J. Meng, and B. Hu, "Characteristic mode analysis of a nonuniform metasurface antenna for wearable applications," *IEEE Antennas and Wireless Propagation Letters*, Vol. 19, No. 8, 1355–1359, 2020.

25. Wang, K., W. Shao, X. Ding, B. Z. Wang, and B. J. Jiang, "Design of high-gain metasurface antenna based on characteristic mode analysis," *IEEE Antennas and Wireless Propagation Letters*, Vol. 21, No. 4, 661–665, 2022.

26. Liu, C., L. Wang, X. Chen, A. Politano, D. Wei, G. Chen, W. Tang, W. Lu, and A. Tredicucci, "Room-temperature high-gain long-wavelength photodetector via optical-electrical controlling of hot carriers in graphene," *Adv. Opt. Mater.*, Vol. 6, 1800836, 2018.

27. Xu, H., C. Guo, J. Zhang, W. Guo, W. Hu, L. Wang, G. Chen, X. Chen, and W. Lu, "PtTe2-based Type-II dirac semimetal and its van der Waals heterostructure for sensitive room temperature terahertz photodetection," *Small*, Vol. 15, 1903362, 2019.